Investigation of Turbulent Airfoil Flow and Slat Noise Mechanisms

D. König, S.R. Koh, M. Meinke, W. Schröder

Institute of Aerodynamics, RWTH Aachen University,

Wüllnerstr. 5a, 52062 Aachen, Germany

Abstract

The flow field and the acoustic field of a high-lift configuration consisting of a slat and a main wing are numerically investigated by a hybrid method. In a first step, the unsteady flow field is computed via a large-eddy simulation (LES) and in a second step, the acoustic field is determined by solving the acoustic perturbation equations (APE). The mean flow field is compared to experimental findings followed by an investigation of the turbulent structures which are visualized by λ_2 contours. A comparison of the numerically obtained pressure spectrum with measurements shows a good agreement in the magnitude and the decay which is found to be approximately f^{-2}. Furthermore, a mixture of broadband and tonal noise between 1 and 3kHz exists in the slat gap region which is identified analyzing correlations between the noise sources and the acoustic pressure.

1 Introduction

Due to the increasing air traffic during the next decade the development of larger aircraft and a higher take-off and landing frequency are expected. Both imply a significantly higher noise exposure to the people living or working near airports whereas the sensitivity concerning noise rises. Therefore, stricter regulations for airplane licenses and night flying restrictions are required. Hence, it is essential for the aviation industry to consider a low-noise design during the aircraft development process.

The generated noise can roughly be divided in engine and airframe noise. Since quite some progress has been made in the reduction of jet noise, airframe noise has become more and more important. Especially during landing, when engines run almost in idle condition, airframe noise is an essential part of the emitted sound. The major contributors of airframe noise are high-lift devices, e.g. slats and flaps, and landing gears. For a low-noise design of these airplane parts a detailed understanding of the underlying sound generating turbulent flow field is required.

In the current work the noise generated by the flow over a high-lift configuration consisting of a slat and a main wing is numerically investigated using an efficient hybrid LES/CAA method. That is, in the first step, a three-dimensional compressible large-eddy simulation is performed to study the unsteady turbulent flow field and to sample data, which is required for the further acoustic analyses. Then, in the second step, the acoustic simulations are based on solutions of the acoustic perturbation equations (APE) [1, 2]. The simulations are done for a flow at a

Mach number of M=0.16 and a Reynolds number, based on the freestream velocity and the clean chord length, of Re=1.4·10^6. The angle of attack is α=13 deg. These flow parameters are related to the experiments of Kolb et al. [3].

The paper is organized as follows. In section 2, the numerical methods and the computational setups of the flow field and the acoustic field are described. Subsequently, in section 3 the results are shown. First, the flow field is analyzed starting with the mean flow properties followed by the evaluation of the turbulent flow structures. Then, the results of the acoustic simulation and the associated post-processed data are discussed. A more thorough discussion is given in [4, 5].

2   Numerical Analysis

The investigation of the unsteady, three-dimensional flow field is done by an explicit flow solver of second order accuracy in space and time. For a detailed description of the numerical methods and a discussion of the accuracy of the LES the reader is referred to [4, 6, 7, 8, 9].

To analyze the acoustic field the acoustic perturbation equations (APE) are used [1]. A thorough discussion of the applied numerical methods can be found in [10, 2, 4].

The computational mesh used for the LES consists of 32 blocks with a total number of 55 million grid points. The spanwise extension of 2.1% of the clean chord length C is resolved by 65 points.

On the far-field boundaries of the computational domain boundary conditions based on the theory of characteristics are applied. An additional sponge layer following [11] is added to these boundaries to avoid spurious reflections, which would harm the acoustic analyses. On the walls, an adiabatic no-slip boundary condition is imposed with a zero pressure gradient normal to the wall. In the spanwise direction periodic boundary conditions are used.

The computation is performed at a freestream Mach number of Ma=0.16 at an angle of attack of 13 deg. The Reynolds number which is based on the clean chord length and the freestream velocity is Re=1.4·10^6.

The acoustic perturbation equations are solved on a two-dimensional domain of 24 blocks which comprises 1,790,146 cells to resolve the acoustic field.

A detailed description of the computational setup is given in [4].

3   Results

3.1   Flow Field

The following section starts with some general information about the LES computation and data sampling. Then, the mean flow field is analyzed and numerical and experimental findings are juxtaposed. Subsequently, the instantaneous turbulent flow structures are investigated followed by a discussion of some turbulence statistics. Finally, the distribution of the major noise source, i.e., the Lamb vector $\mathbf{L} = \boldsymbol{\omega} \times \mathbf{u}$ being defined as the cross product of the vorticity vector and the velocity vector is analyzed. A more detailed and thorough discussion is given in [4, 5].

The simulation has been run for approximate 5 non-dimensional time units based on the freestream velocity u_∞ and the clean chord length C to sample unsteady flow data at a time interval of approximately 0.0015 time units.

The Mach number distribution and some selected streamlines of the time and spanwise averaged flow field are depicted in Fig. 2. It is evident that the slat cove region is an area of

very low Mach number, which is characterized by a strong recirculation being illustrated by the streamlines. This recirculation area is separated from the flow passing the slat gap by a shear layer, which emanates at the slat cusp. Shortly downstream of the slat gap the high Mach numbers mark the pronounced suction region on the main wing. In Fig. 3 the result of a monoscopic particle-image velocity (PIV) measurement is shown.

It is obvious that regarding the overall flow structure, i.e., the location of the stagnation point on the main wing, the size of the cove vortex and its center position, and the shape of the shear layer covering the cove vortex, of the computational and experimental findings on the pressure side are in very good agreement. The unusual distribution between the slat cusp and the main wing stagnation point is due to some diffuse reflections being caused by the support to position the slat.

Figures 4 to 7 show the LES and experimental velocity distribution on the lines A, B, C, and D as a function of the non-dimensional coordinate s. The locations of these lines are defined in Fig. 2. The discrepancy near the wall and in the recirculation region visible in Figs. 5 and 6 is caused by too few seeding particles in this region in the measurements. This is true upstream of the cusp and also inside the cove. Further off the wall, the numerical and experimental results are in very good agreement. Especially, the peak values which indicate the location of the shear layer do coincide. Figure 5 shows that the large-eddy simulation and the PIV measurement determine recirculation zones of approximately the same size in the slat cove.

Since the vortex-vortex and vortex-wall interaction is extremely important for the noise generation process the unsteady turbulent structures in the slat region will be investigated in detail. The vortical structures are visualized by λ_2 contours [12]. Figure 8 illustrates the overall development of the vortical structures in the boundary layers of the slat and of the main airfoil, downstream of the slat trailing edge, and in the slat cove region. The grey scales mapped onto the λ_2 contours visualize the Mach number distribution.

The recirculation zone in the slat cove is bounded by the turbulent shear layer emanating from the slat cusp and reattaching near the slat trailing edge. Immediately downstream of the cusp the shear layer possesses two-dimensional, spanwise oriented vortex structures. These rollers result from the velocity profile in the shear layer and the associated Kelvin-Helmholtz instability [13]. Figure 9 shows the λ_2 contours near the slat cusp where these spanwise rollers occur. Furthermore, the vortical structures from the slat cove recirculation area penetrate into the shear layer and distort the rollers. This mixing and interaction of shear layer structures with structures from the recirculation area seem to enhance secondary instabilities which lead to the development of streamwise oriented vortical structures between two rollers. Similar structures which are termed rib vortices have been described e.g. in [13, 14].

Figure 10 shows some rollers and rib vortices shortly before the shear layer enters the reattachment area. Also note the sinusoidal appearance of the rollers, the rollers develop a slightly curved or wavy shape, respectively, due to their interaction with the rib vortices.

Furthermore, Fig. 10 illustrates some more pronounced vortices in the reattachment region, whose axes are aligned with the streamwise direction. These structures seem to be generated by the sinusoidal form of the spanwise rollers and by the convection of the rib vortices which are highly stretched by the accelerated slat gap flow. It is obvious that the parts of the rollers extending into this accelerated flow region undergo a stronger deformation leading to a pronounced distortion of the rollers such that they finally collapse. The remaining structures are predominantly aligned with the streamwise direction.

In the following some turbulence statistics are presented. First, the distribution of the turbulent kinetic energy $k = \frac{1}{2}\left(u'^2 + v'^2 + w'^2\right)/u_\infty^2$ is shown in Fig. 11. High k values occur in the shear

layer, the recirculation area, and in the wake of the slat trailing edge. The peak value of k is produced by the reattaching shear layer where the flow is split into a recirculation part, i.e., the slat-cove vortex, and a slat-gap-shear-layer part. A similar distribution of the turbulent kinetic energy with likewise locations for the local maxima of k is reported in [15].

The analysis of the turbulent structure of the slat-gap flow is based on the anisotropy-invariant map [16]. Figure 12 shows the results for several points along a grid line approximately perpendicular to the slat wall and located in the slat-gap region. The position of the points is indicated by the thick solid line in Figs. 13 to 15. The origin of the map defines isotropic turbulence. The other two vertices represent isotropic two-component turbulence (left vertex) and one-component turbulence (right vertex). The curve connecting the origin and the left vertex defines axisymmetric turbulence the statistical properties of which are invariant under rotation around one axis with fluctuation intensities along the axis of rotation being smaller than in the remaining directions. The curve between the origin and the right vertex represents axisymmetric turbulence with fluctuation intensities along the axis larger than in the other directions. The connection of the left and the upper vertex defines two-component turbulence. It is noticeable, that the points close to the wall are characterized by two-component turbulence which is typical for wall bounded flows. Moving away from the wall the turbulence becomes axisymmetric with one pronounced fluctuating velocity component and further off the surface axisymmetric with two distinct components. This structure is determined by the above described streamwise orientated vortical structures just downstream of the slat cove shear layer reattachment point which induce velocity fluctuations in the wall normal and spanwise direction whereas the wall normal fluctuations close to the wall are highly damped. This statement is substantiated by the high values of the spanwise $\overline{w'w'}$ component in Fig. 15 of the Reynolds stress tensor close to the wall. Compared to this spanwise component the components parallel to the slat wall $\overline{u'u'}$ (Fig. 13) and normal to the slat wall $\overline{v'v'}$ (Fig. 14) are extremely small. Further away from the wall the $\overline{v'v'}$ component reaches the same value as the $\overline{w'w'}$ component. The overall small $\overline{u'u'}$ can be explained by the small variation of the streamwise velocity u in the slat-gap. That is, there is hardly any the difference of the streamwise velocity u on its way through the gap and therefore u' is small.

Finally, the distribution of the major source term generating the acoustic field is shown. When airframe noise is considered this major source is described by the Lamb vector $\mathbf{L} = \boldsymbol{\omega} \times \mathbf{u}$ [2]. Figure 16 shows a snapshot of the norm of the spanwise perturbed Lamb vector. It is obvious that the strongest sources occur in the regions with the highest vortical activity and the highest turbulent kinetic energy (cf. Fig. 11), i.e., in the shear layer, the reattachment area, and the slat wake.

As far as the flow field is concerned it has been shown that the large-eddy simulation results are in good agreement with the experimental findings. A detailed investigation of the turbulent structures of the slat cove shear layer visualized by λ_2 contours revealed the periodic occurrence of spanwise orientated rollers and streamwise aligned rib vortices. Just before the shear layer impinges on the slat trailing edge these structures undergo a strong deformation due to the highly accelerated slat gap flow. The resulting vortex-vortex interaction and vortex-wall interaction are expected to be responsible for the generation of tonal components in the acoustic frequency spectrum. A detailed investigation of the sound generated by the above discussed turbulent flow field is given in the following section and in [4, 5].

3.2 Acoustic Field

Based on the LES solution of the turbulent wall-bounded flow, where the motion of the vortical structures determines the effective acoustic source, the near far-field acoustics is computed by the APE-4 system. A schematic view of the present computational setup is shown in Fig. 1. The data processing for the acoustic simulation is based on 3750 LES samples at a time step $0.009C/c_\infty$. The acoustic computations are run for a non-dimensional time period of $34.2C/c_\infty$. During this time interval the acoustic waves initiated in the slat region propagate a distance six times larger than the maximum extent of the computational domain.

In the Figs. 17 to 19 the acoustic field generated by the turbulent flow over the slat-wing configuration is shown. In the slat region strong acoustic pulses are generated by the vortical structures in the slat cove and high frequency waves are produced by the turbulent shear layers passing over the trailing edge of the main wing. The wavelength of this high frequency acoustics is about $\lambda \approx 0.14C$, which corresponds to a frequency $f = (c_\infty - U_\infty)/\lambda$ of approximately 5kHz when the pressure wave propagates upstream.

The computed sound spectra at the four locations 'P1' to 'P4' which are defined in Table 1 and Fig. 1, respectively, are presented in Fig. 20 and compared with experimental findings. According to the previous investigation [3] the sound spectra at the near far-field have two

Table 1: Location of the artificial microphones in the acoustic field.

Microphone No.	P1	P2	P3	P4
$||\boldsymbol{r}||/C$	3.4	3.4	3.5	3.7
θ (degree)	-70	-62	-53	-44

features. The first feature is the broadband noise to form an f^{-2} dependence due to the turbulence of the wall-bounded shear layers. The second characteristic property is the discrete tones induced by aerodynamic interactions between the wall shear-layer and the solid wall and by the vortex-vortex interaction. At 5kHz an acoustic hump is observed due to the trailing edge noise which has been discussed in the context of Fig. 16 and whose wavelength is indicated in Fig. 17.

Next, the dominant noise structures are analyzed which can be determined by a cross-correlation function R_{AB} between far-field acoustics and turbulent flow motion. For a detailed description of the cross-correlation used in the present investigation the reader is referred to [4, 5].

In a first analysis the cross-correlation function is computed using the original acoustic signal and in another investigation a filtered version of this signal is used. That is, a band-pass filter of shape factor 1.2:1 at 30/3dB is applied to the frequency domain and subsequently, the filtered signal is transformed back into the time domain. In the presented study a 2kHz band-pass filter at the center frequency of 2kHz is used which leads to an acoustic pressure signal containing only tonal and broadband components between 1kHz and 3kHz.

The cross-correlations between the near-field noise source and the original acoustic signal and the filtered acoustic signal, respectively, at microphone position 'P3' are juxtaposed in Figures 21 to 24 for several retarded times τ. For the original acoustic pressure signal correlations occur at all retarded times in regions of high turbulence. Unlike the distribution of the original acoustic pressure signal the filtered acoustic pressure signal shows significant values of the correlation function $R_{AB}(\xi, \tau)$ only at a time shift of about $\tau \approx 3.5$. These peak values occur between the reattachment area of the slat cove shear layers and the leading edge of the main

wing. Hence, the tonal and broadband noise in the range of 1kHz to 3kHz is mainly generated in the slat gap region. The comparison of Fig. 23 and Fig. 11 evidences that the region where the correlation peaks does not exactly coincide with the location where the maximum turbulent kinetic energy occurs. The reason for this behavior is caused by the vortical structures which impinge upon the slat surface and generate strong pressure fluctuations. These fluctuations are reflected on the surface of the main wing. According to a numerical investigation by Tam and Pastouchenko [17] the periodic shedding of vortices is linked to an acoustic feedback loop by the pressure pulse impinging upon the opposite surface. When the frequency of the noise source matches that of the feedback modes, a strong tone is generated by the acoustic resonance [18]. In other words, an acoustic resonance is initiated due to the slat gap boundaries. In the present slat flow the periodic vortex shedding from the slat cusp can trigger the generation of such an acoustic pulse. The cross-correlation of the noise source term ($\mathbf{L}'$), which includes the solenoidal vortical perturbation and the acoustic perturbation [1], expresses the noise generation due to a fluid-acoustic feedback mechanism.

The cross-correlations at four locations in the slat gap are presented in Fig. 25. The distances from the trailing edge of the slat are $1.6h$, $4.2h$, $10.5h$, and $14.6h$, respectively, where h is the thickness of the trailing edge of the slat. The minimum distance to the surface of the main wing is about $30h$. The pronounced correlation peak is obtained for the location 'c' at a time difference of $3.5C/c_\infty$ which corresponds to the time required by a wave traveling at the speed of sound to reach the microphone position 'P3'. This agreement with the wave propagation time evidences the immediate relation with the noise generation due to the slat gap and the pressure pulse enhanced by a periodic interaction with a solid surface.

It can be concluded that periodic turbulent shear layer structures determine the noise components between 1kHz to 3kHz. Therefore, a low noise design may be achieved by modifying the shear layer, e.g., by active flow control mechanisms, such that the periodicity in the shear layer is suppressed.

4   Conclusions

The flow field and the acoustic field of turbulent flow over a slat-wing configuration have been analyzed. The Reynolds number based on the clean chord length C has been Re=$1.4 \cdot 10^6$ and the freestream Mach number has been Ma=0.16. The numerical method has been based on a hybrid LES/CAA approach, i.e., first, the flow field has been computed by a large-eddy simulation and then, the acoustic field has been determined by solving the acoustic perturbation equations in the APE-4 form.

The time averaged flow field computed by the second-order accurate LES has been shown to be in good agreement with the experimental pressure and velocity distributions. High areas of turbulent kinetic energy have been observed in the slat cove shear layer, the recirculation area, and in the wake of the slat trailing edge. The analysis of the unsteady flow structures, visualized by λ_2 contours, evidences the periodic occurrence of rollers and rib vortices in the shear layer. When these structures reach the reattachment point of the shear layer slightly upstream of the slat trailing edge, they are partly destroyed and convected through the slat gap. In the immediate vicinity of this reattachment region the turbulent kinetic energy reaches its maximum. The analysis of the anisotropy invariant map shows the axisymmetric structure of the turbulence in the gap region.

The acoustic field determined by the hybrid LES /CAA approach is in convincing agreement with the measurements. The sound spectra in the near far field have two characteristic proper-

ties. The first characteristic is the typical broadband noise due to wall-bounded turbulence, i.e., the corresponding acoustics is proportional to f^{-2}. The second eminent property is the tones induced by the aerodynamic interaction between the wall shear layer and the solid surface, i.e., several tones are generated over a frequency range of 1kHz to 3kHz. The tones in the frequency range below 3kHz are related to the slat gap, the size of the recirculation zone, and the wake of the trailing edge of the slat. The trailing edge of the main wing generates a high frequency tone at 5kHz.

Based on the cross-correlation between the acoustic signal which is determined by the solution of the APE-4 equations and the noise source which is obtained by the large-eddy simulation, the present analysis shows the main vortex sound source to be the shear layer which emanates from the slat cusp and impinges upon the lower slat surface. Furthermore, the cross-correlation analysis identifies the fluid-acoustics mechanism in the slat-gap region to be generated by the pressure wave pulsating between the slat trailing edge and the main wing surface. This pulsation is triggered by the spatial fluctuation of the impingement point of the shear layer which covers the cove vortex.

From these findings it could be concluded that active flow control seems to be a reasonable means to suppress the periodicity in the shear layer and to lower slat noise.

References

[1] Ewert, R. and Schröder, W., "Acoustic Perturbation Equations Based on Flow Decomposition via Source Filtering," *J. Comput. Phys.*, Vol. 188, 2003, pp. 365–398.

[2] Ewert, R. and Schröder, W., "On the simulation of trailing edge noise with a hybrid LES/RANS method," *Journal of Sound and Vibration*, Vol. 270, 2004, pp. 509–524.

[3] Kolb, A., Faulhaber, P., Drobietz, R., and Grünewald, M., "Aeroacoustic Wind Tunnel Measurements on a 2D High-Lift Configuration," *13th AIAA/CEAS Aeroacoustics Conference AIAA*, AIAA Paper 2007-3447, 2007.

[4] König, D., Koh, S. R., Meinke, M., and Schröder, W., "Two-Step Simulation of Slat Noise," *Computers and Fluids*, Vol. 39, No. 3, 2010, pp. 512–524.

[5] König, D., Koh, S. R., Schröder, W., and Meinke, M., "Slat Noise Source Identification," *15th AIAA/CEAS Aeroacoustics Conference (30th AIAA Aeroacoustics Conference)*, AIAA Paper 2009-3100, 2009.

[6] Meinke, M., Schröder, W., Krause, E., and Rister, T., "A Comparison of Second- and Sixth-Order Methods for Large-Eddy Simulations," *Computers and Fluids*, Vol. 31, 2002, pp. 695–718.

[7] Rütten, F., Schröder, W., and Meinke, M., "LES of Frequency Oscillations of the Dean Vortices in Turbulent Pipe Bend Flow," *Physics of Fluids*, Vol. 17, No. 2, 2005.

[8] Alkishriwi, N., Schröder, W., and Meinke, M., "A Large-Eddy Simulation Method for Low Mach Number Flows Using Preconditioning and Multigrid," *Computers and Fluids*, Vol. 35, No. 10, 2006, pp. 1126–1136.

[9] Renze, P., Schröder, W., and Meinke, M., "LES of turbulent mixing in film cooling flows," *Flow, Turbulence and Combustion*, Vol. 80, 2008, pp. 119–132.

[10] Schröder, W., Ewert, R., Bui, T. P., and Gröschel, E., "An LES-APE Approach in Computational Aeroacoustics: Theory and Applications," Computational Aeroacoustics VKI Lecture Series 2006-05, 2006.

[11] Israeli, M. and Orszag, S. A., "Approximation of Radiation Boundary Conditions," *J. Comput. Phys.*, Vol. 41, 1981, pp. 115–135.

[12] Jeong, J. and Hussain, F., "On the identification of a vortex," *J. Fluid Mech.*, Vol. 285, 1995, pp. 69–94.

[13] Rogers, M. M. and Moser, R. D., "The three-dimensional evolution of a plane mixing layer: the Kelvin-Helmholtz rollup," *J. Fluid Mech.*, Vol. 243, 1992, pp. 183–226.

[14] Sakakibara, J., Hishida, K., and Phillips, W. R. C., "On the vortical structure in an plane impinging jet," *J. Fluid Mech.*, Vol. 434, 2001, pp. 273–300.

[15] Choudhari, M. M. and Khorrami, M. R., "Slat Cove Unsteadiness: Effect of 3D Flow Structures," *44st AIAA Aerospace Sciences Meeting and Exhibit*, AIAA Paper 2006-0211, 2006.

[16] Lumley, J. L., "Computational modeling of turbulent flows," *Adv. Appl. Mech.*, Vol. 18, 1978, pp. 123–176.

[17] Tam, C. K. W. and Pastouchenko, N., "Gap tones," *AIAA J.*, Vol. 39, No. 8, 2001, pp. 1442–1448.

[18] Hein, S., Hohage, T., and Koch, W., "On resonance in open systems," *J. Fluid Mech.*, Vol. 506, 2004, pp. 255–284.

Figures
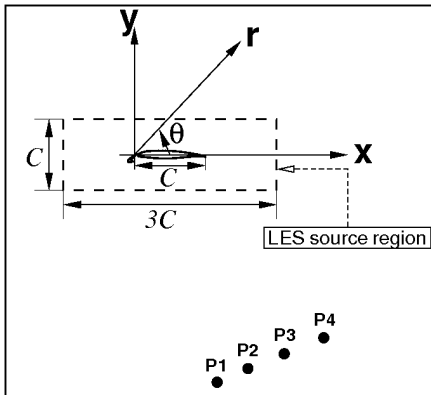
Figure 1: Schematic of the acoustic domain including the definition of the microphone positions.
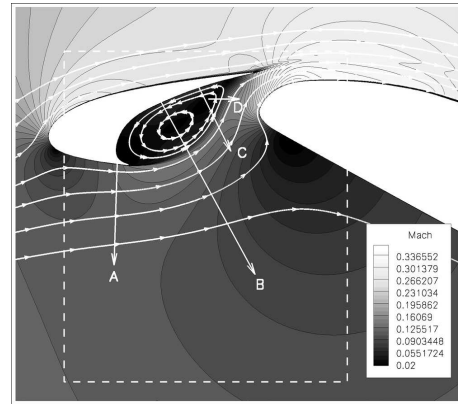
Figure 2: Streamlines and Mach number contours of the time and spanwise averaged LES flow field data. The dashed box marks the section shown in Fig. 3. The velocity distributions normal to the lines A, B, C, and D as a function of the normalized coordinate s along these lines are shown in Figs. 4 to 7.
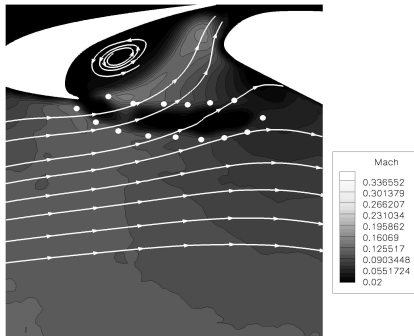
Figure 3: Streamlines and Mach number contours of the PIV measurement. The dotted area marks the location of the slat strake to fix the position of the slat.
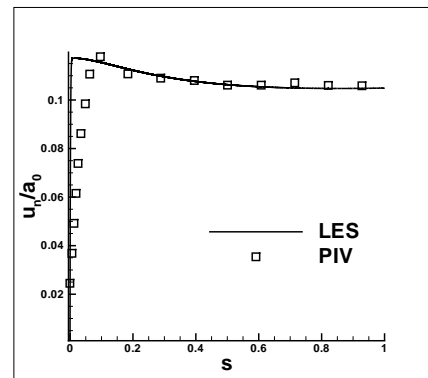
Figure 4: Velocity profile along line A, which is defined in Fig. 2, as a function of the normalized coordinate s along this line; comparison of LES and PIV data.
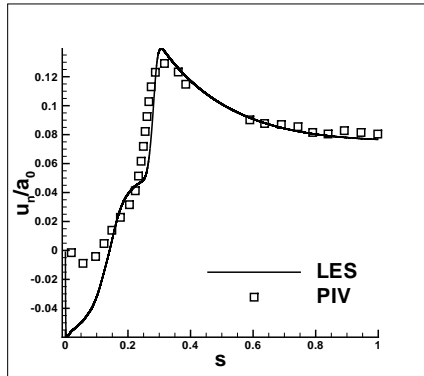
Figure 5: Velocity profile along line B, which is defined in Fig. 2, as a function of the normalized coordinate s along this line; comparison of LES and PIV data.
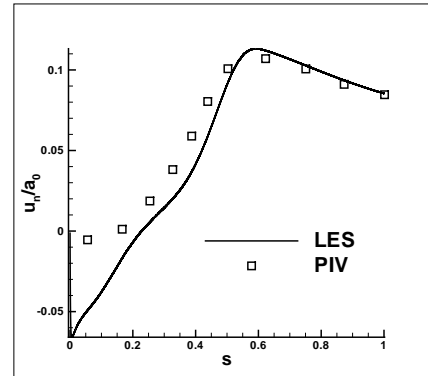
Figure 6: Velocity profile along line C, which is defined in Fig. 2, as a function of the normalized coordinate s along this line; comparison of LES and PIV data.
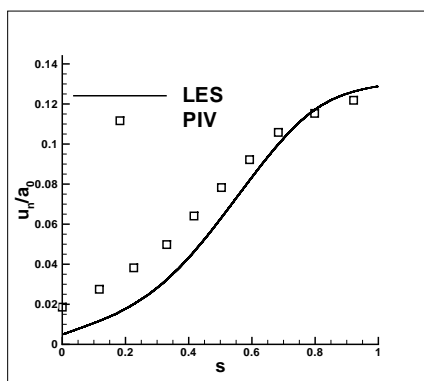
Figure 7: Velocity profile along line D, which is defined in Fig. 2, as a function of the normalized coordinate s along this line; comparison of LES and PIV data.
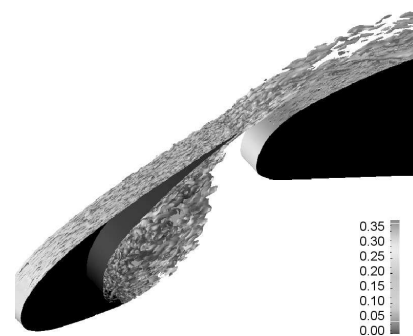
Figure 8: Turbulent structures in the slat area visualized by λ_2 contours with mapped on Mach number distribution.
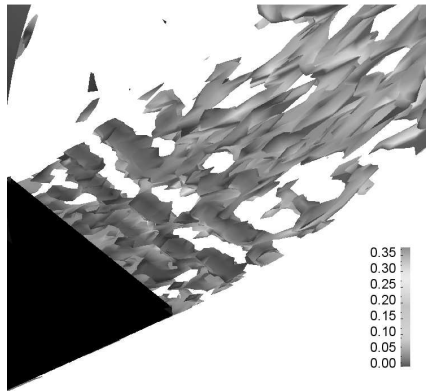
Figure 9: Development of rollers downstream of the slat cusp and penetrating vortical structures from the recirculation area visualized by λ_2 contours.
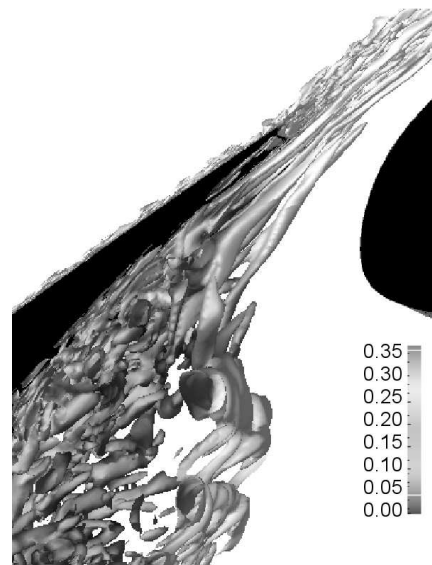
Figure 10: Vortical structures in the reattachment area of the slat cove shear layer visualized by λ_2 contours.
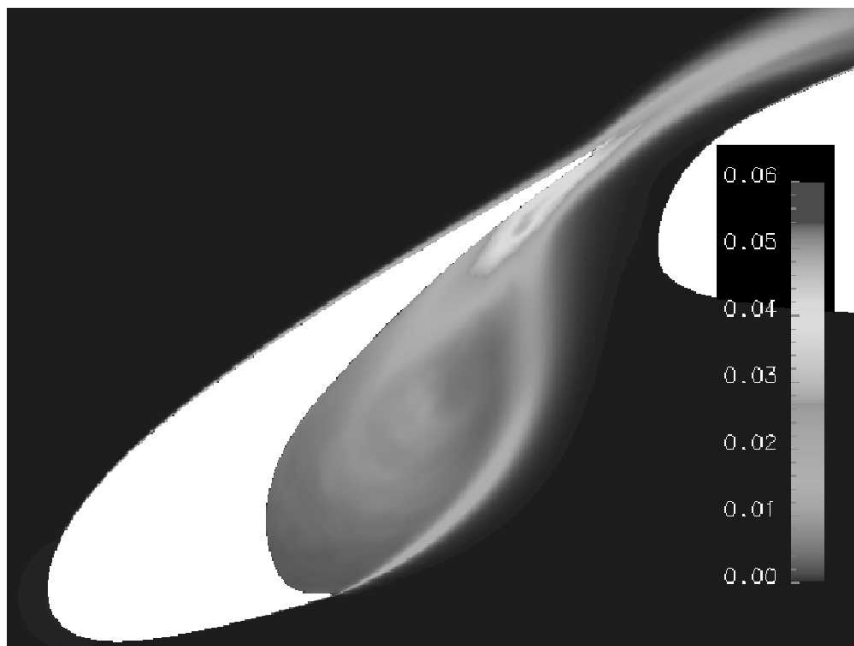
Figure 11: Turbulent kinetic energy k non-dimensionalized by u_∞^2 in the slat region.
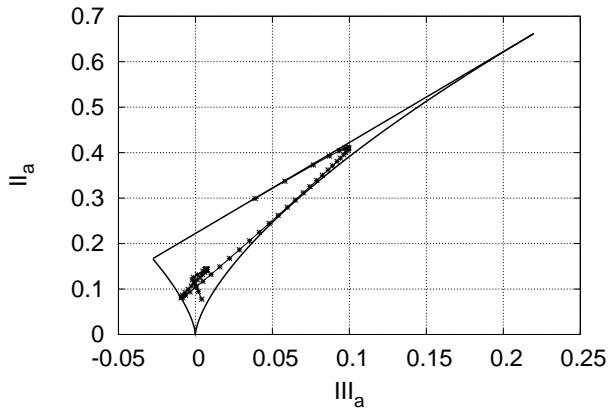
Figure 12: Anisotropy-invariant map for several points along a grid line normal to the slat wall located in the slat-gap region; the thick solid line in Figs. 13, 14, 15 defines locations of the points.
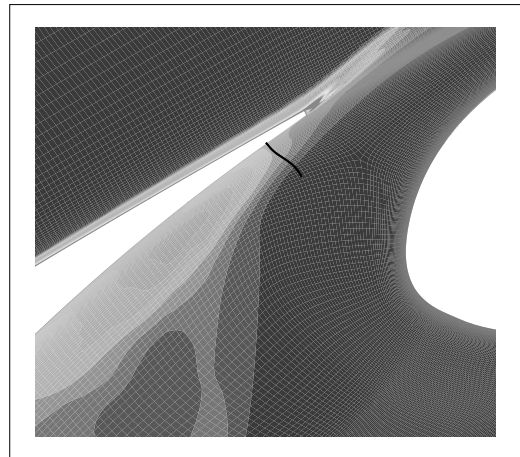
Figure 13: $\overline{u'u'}$ component of the Reynolds stress tensor. Black line marks the points extracted for the anisotropy-invariant map.
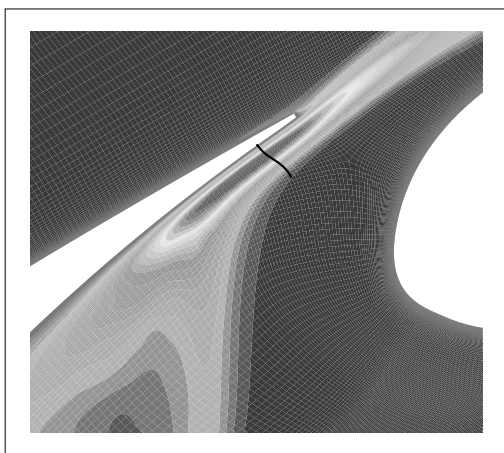
Figure 14: $\overline{v'v'}$ component of the Reynolds stress tensor. Black line marks the points extracted for the anisotropy-invariant map.
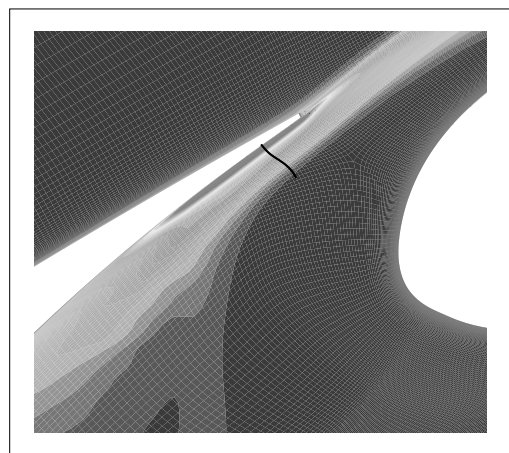
Figure 15: $\overline{w'w'}$ component of the Reynolds stress tensor. Black line marks the points extracted for the anisotropy-invariant map.
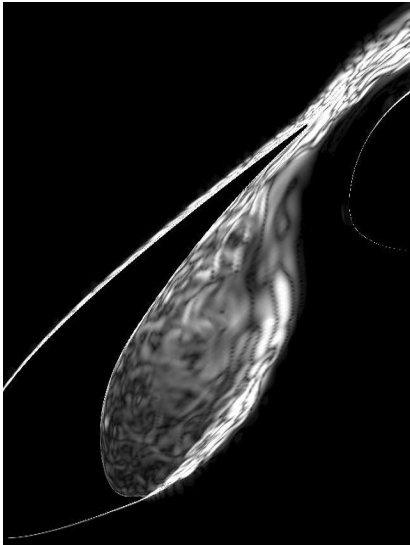
Figure 16: Snapshot of the norm of the spanwise averaged perturbed Lamb vector in the slat region.
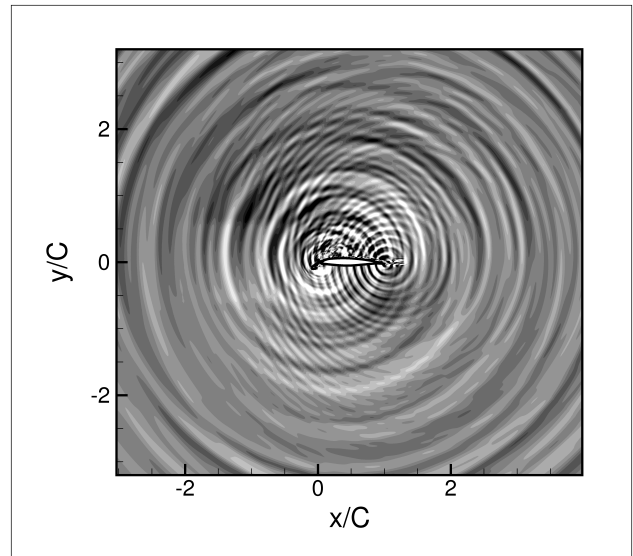
Figure 17: Acoustic pressure contours determined by the APE-4 system.
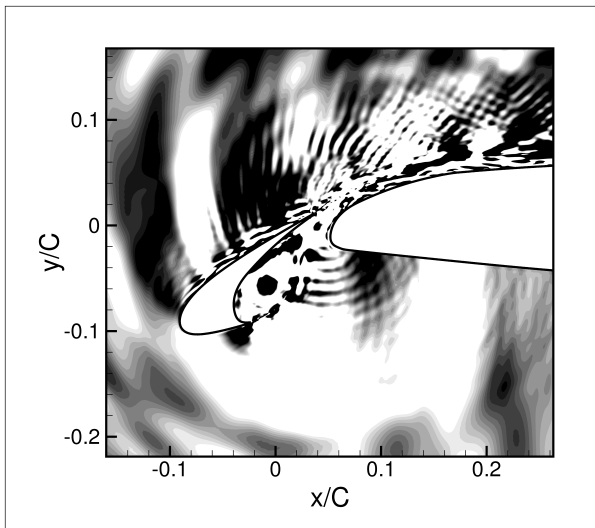
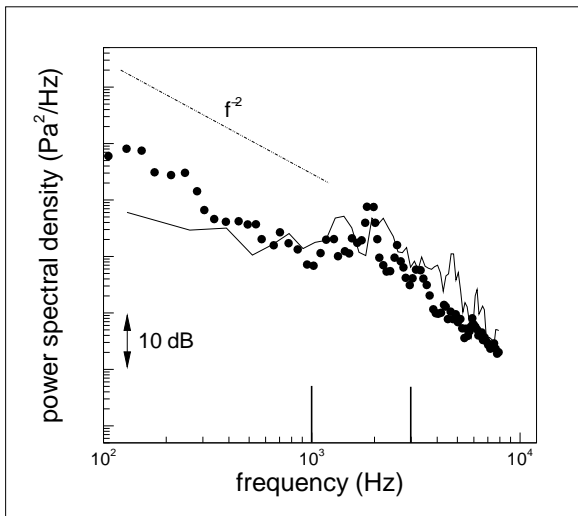Figure 18: Acoustic pressure contours in the slat region determined by the APE-4 system.
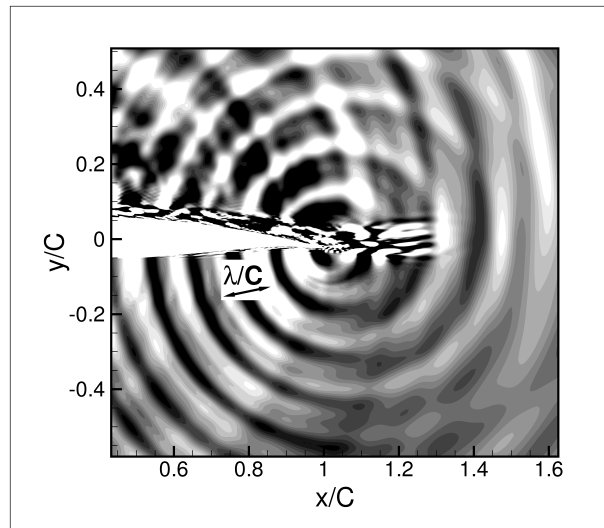
Figure 19: Acoustic pressure contours at the trailing edge of the main wing determined by the APE-4 system.
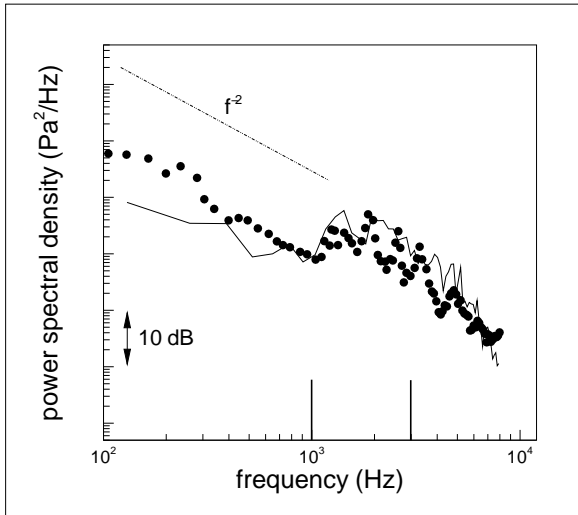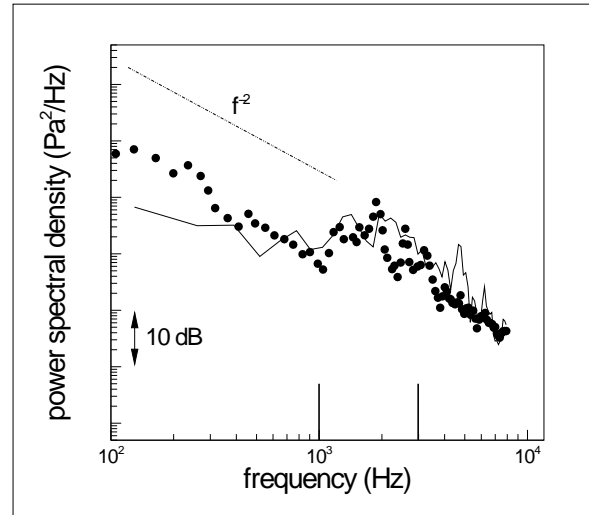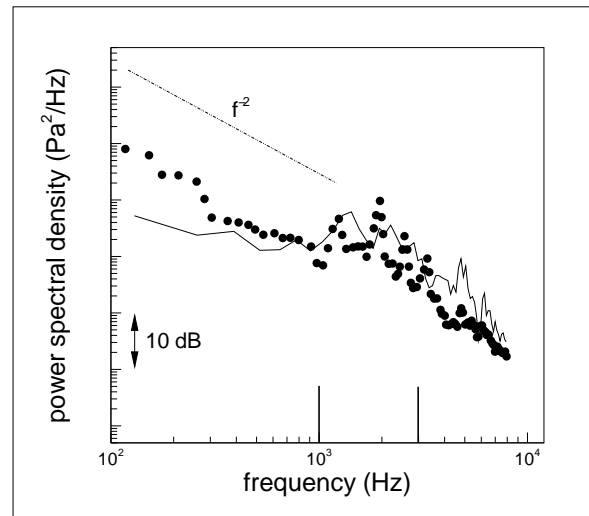
Figure 20: Sound spectra at the near farfield locations. Solid line: computation, symbol: experiment. Vertical lines mark the 1 to 3kHz range in which tonal and broadband noise is noticeable.
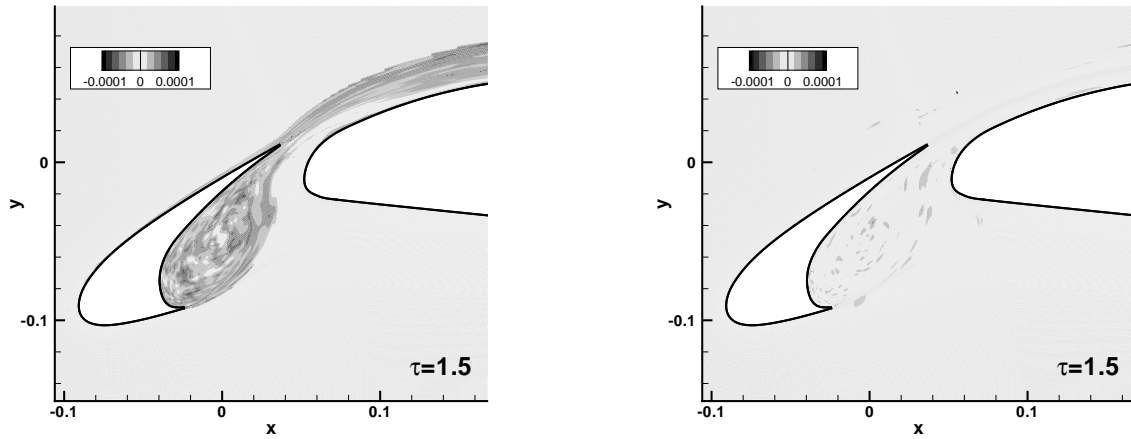
Figure 21: Cross-correlation contours of $R_{AB}(\boldsymbol{\xi}, \tau = 1.5)$ determined by the acoustic source $|L'|$ and the acoustic pressure p' at the microphone position 'P3'. Left: original acoustic pressure signal. Right: filtered acoustic pressure signal.
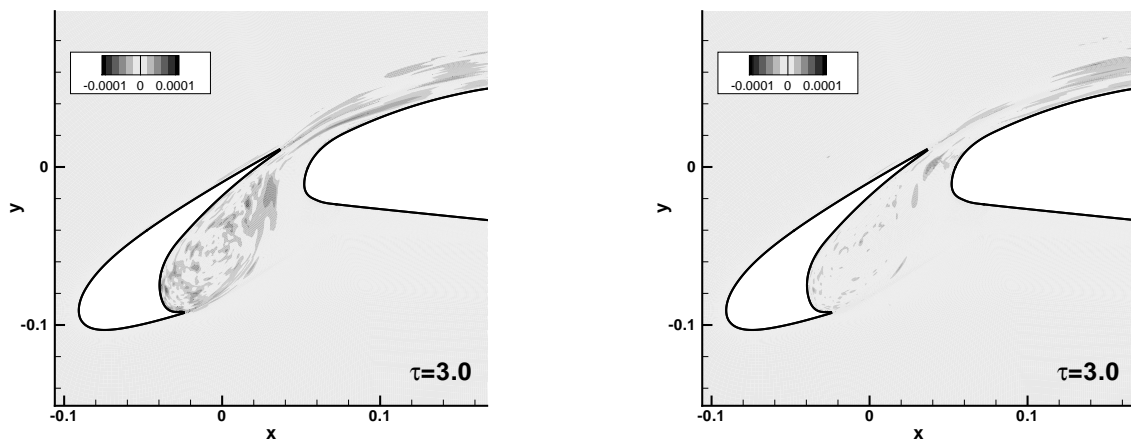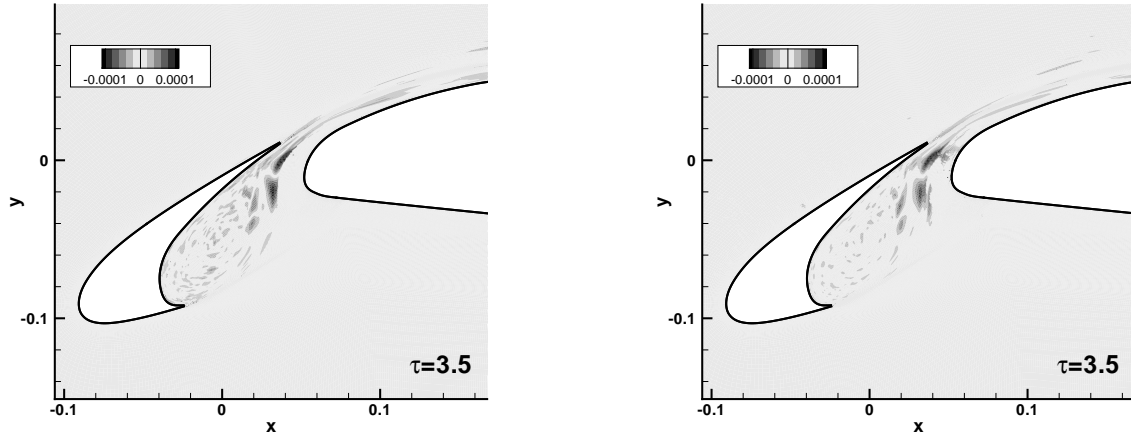

Figure 22: Cross-correlation contours of $R_{AB}(\boldsymbol{\xi}, \tau = 3.0)$ determined by the acoustic source $|L'|$ and the acoustic pressure p' at the microphone position 'P3'. Left: original acoustic pressure signal. Right: filtered acoustic pressure signal.

Figure 23: Cross-correlation contours of $R_{AB}(\boldsymbol{\xi}, \tau = 3.5)$ determined by the acoustic source $|L'|$ and the acoustic pressure p' at the microphone position 'P3'. Left: original acoustic pressure signal. Right: filtered acoustic pressure signal.
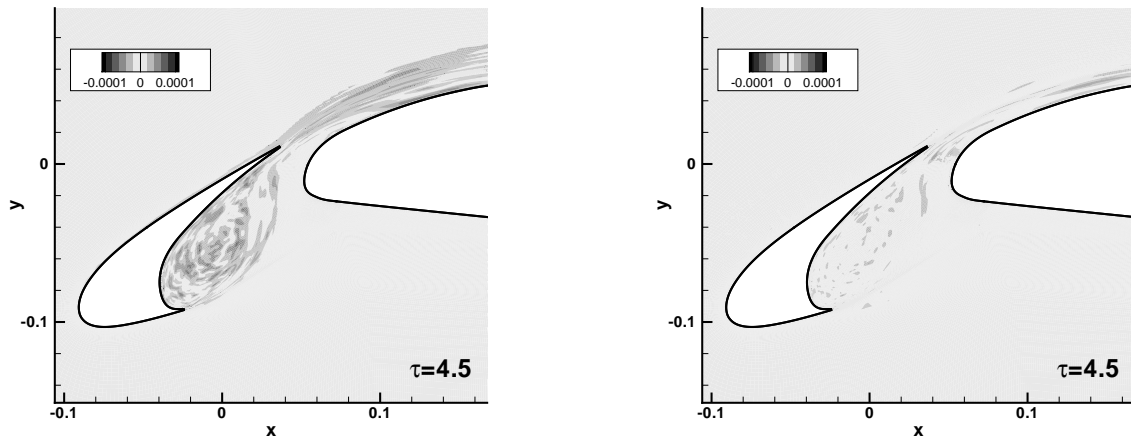

Figure 24: Cross-correlation contours of $R_{AB}(\boldsymbol{\xi}, \tau = 4.5)$ determined by the acoustic source $|L'|$ and the acoustic pressure p' at the microphone position 'P3'. Left: original acoustic pressure signal. Right: filtered acoustic pressure signal.
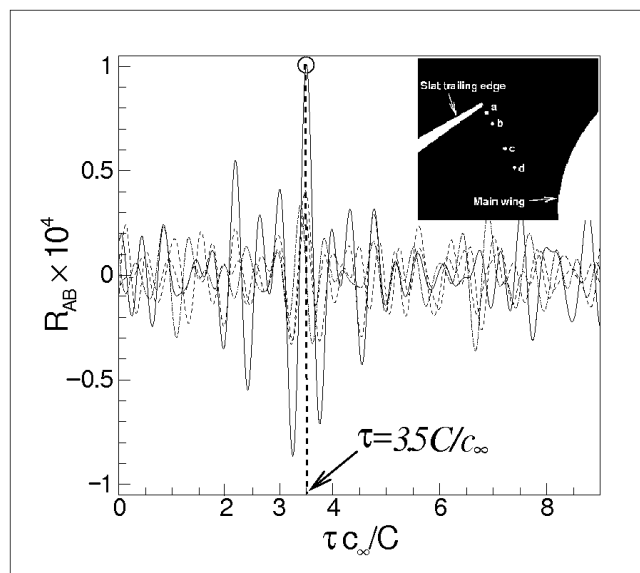
Figure 25: Temporal distribution of R_{AB} at four locations 'a' $\cdots$, 'b' $-\cdot-$, 'c' ——, 'd' $---$, which are defined in the upper subfigure.